Research Square

Preprints are preliminary reports that have not undergone peer review.
They should not be considered conclusive, used to inform clinical practice,
or referenced by the media as validated information.

Electrical Performance of Cement Nanofiller Composites for Low-Grade Thermoelectric Energy Harvesting

Thakur Ramjiram Singh
Birla Institute of Technology and Science, Pilani
Shiv Singh
Advanced Materials and Processes Research Institute
Subhasis Pradhan
Subhasis.pradhan@pilani.bits-pilani.ac.in

Birla Institute of Technology and Science, Pilani
Dheerendra Singh
Birla Institute of Technology and Science, Pilani

Research Article

Keywords: Urban heat Island effect, Thermoelectric cement composites, electrical conductivity, carbon-based nanofillers, Candle soot, carbon nanoparticles

Posted Date: August 19th, 2026

DOI: https://doi.org/10.21203/rs.3.rs-10278550/v1

License: This work is licensed under a Creative Commons Attribution 4.0 International License.
Read Full License

Additional Declarations: No competing interests reported.

Electrical Performance of Cement Nanofiller Composites for Low-Grade Thermoelectric Energy Harvesting

Thakur Ramjiram Singh[1], Subhasis Pradhan[1*], Shiv Singh[2*], Dheerendra Singh[3]

[1]Department of Civil Engineering, Birla Institute of Technology & Science Pilani, Pilani Campus, Rajasthan - 333 031, India. *p20220418@pilani.bits-pilani.ac.in*

[2]Council of Scientific and Industrial Research - Advanced Materials and Processes Research Institute, Bhopal, Madhya Pradesh - 462026, India *sshiv.ampri@csir.res.in*

[3]Department of Electrical Engineering, Birla Institute of Technology and Science Pilani, Pilani Campus, Rajasthan- 333 031, India *dhs@pilani.bits-pilani.ac.in*

**Corresponding authors: Subhasis.pradhan@pilani.bits-pilani.ac.in , sshiv.ampri@csir.res.in*

Abstract: Waste heat, causing the urban heat island effect, can be channelized for the generation of low-grade waste heat from pavements and building envelopes with the use of appropriate material. Cement is a key ingredient in modern infrastructure; studies have shown that adding carbon-based nanofillers can turn it into a conductor. In the present study, the inclusion of super-grade graphene (SGG), multi-walled carbon nanotube (MWCNT), and carbon soot-based carbon nanoparticles (CNP) developed a conductive network. Significant improvement in electrical conductivity and formation of conductive pathways are evident from SEM, XRD, Raman spectroscopy, and electrical conductivity analysis. Moreover, the samples exhibited a denser microstructure. The wet method is used to cast the samples. The Four-point probe method is used to investigate electrical performance. Electrical conductivity of 0.07 S/cm at 2% dose of SGG at 60°C, 0.25 S/cm at 15% dose of MWCNT at 60°C, and 0.03 S/cm at 5% CNP at 85°C is displayed by the respective samples. Percolation threshold, tunnelling, and hopping contribute to a jump in electrical conductivity.

Keywords: Urban heat Island effect, Thermoelectric cement composites, electrical conductivity, carbon-based nanofillers, Candle soot, carbon nanoparticles

1. Introduction

Currently, more than 85% of fossil fuels are utilized as the main source of energy(Yang et al. 2018; Yao et al. 2019). A major portion (more than 65%) of energy is wasted through low- and high-grade industrial heat. In the global context, there is a strong demand for green energy (Yan et al. 2017). Urban development has led to rising temperatures and reduced green cover, resulting in the urban heat island effect (UHI) and global warming. In summer and winter, population density exacerbates energy costs, greenhouse gas emissions, and environmental pollution due to excessive energy use. Low-grade heat stored in asphalt pavement surfaces and concrete structures can be harnessed as green energy and has become the focus of interdisciplinary research (Zhao et al. 2013; Moure et al. 2016; Ahmad et al. 2019; Vizzari et al. 2021; Wei et al. 2021b; Khasawneh 2025).

Pavements are vast surfaces that capture a large share of the solar energy. To collect the energy, the following two aspects are considered. Firstly, photovoltaic power generation technology(Zhou et al. 2015), and secondly, thermoelectric conversion technology. Although Photovoltaic technology is widely used, the main problems are the need for exclusive space and continuous maintenance. Additionally, the recycling and replacement of damaged solar panels causes an environmental burden. Thermoelectricity, a method of generating electricity from temperature difference, has emerged as one of the most promising approaches (Zhang et al. 2019; Carraro et al. 2021). Thermoelectric technology can directly convert outdoor heat into electrical energy without altering the infrastructure (Jiang et al. 2017). For thermoelectric conversion technology, a low power generation efficiency is the main technical challenge, which depends on the thermoelectric performance of the road surface materials (Wei et al. 2014). So far, thermoelectric technologies have not been widely adopted due to various technical limitations, including the harvesting and utilisation of continuous waste heat and filler material knowledge (Duarte and Ferreira 2016).

Cement composites are an attractive alternative for storing waste heat energy due to their vast surface area, affordability, and widespread presence in urban areas. Nevertheless, cement composites exhibited limited electrical conductivity. Hence, it is desirable to fabricate cement and cement-based structures with additional functionalities (Singh et al. 2021). This has to be modified by connecting continuous networks to allow the flow of electrons and holes, thereby enhancing the thermoelectric behaviour (Mendes et al. 2019).

Sun *et al.*(Sun M, Li Z, Mao Q 1998; Mingqing et al. 1999) are the first to explore Portland cement as a matrix, and conductive carbon fibres as a conductive phase, leading to electrical conductivity in the carbon fibre cement composites. From 1998 to 2011, various researchers incorporated different macroscopic conductive phases, such as metal oxides, iron slag, graphite, and carbon fibre, to enhance the electrical properties (Wen and Chung 2000, 2002; Cao et al. 2011; Li et al. 2026). From 2011 to 2020, micro- and nanoscale conductive fillers, such as carbon fibre, expanded graphite, carbon nanotubes, and graphene nanoplatelets, have been incorporated to enhance electrical conductivity (Zuo et al. 2015; Wei et al. 2018b, 2021a; Ghosh et al. 2019). Nanofillers are more effective at enhancing electrical properties than macro- and micro-fillers (Ghosh et al. 2019).

The addition of carbon nanotubes (CNT) at a higher concentration to cement composites generates an electrical conductivity of 0.818 S/cm (Wei et al. 2018a). Zuev *et al.* examined the inclusion of graphene in cement composites and found that the majority charge carrier shifts from electrons to holes (Zuev et al. 2009). When the N-type $CaMnO_3$ thermoelectric module is used, a maximum voltage of 581.7 mV is obtained with a 120-Thermoelectric unit connection (Maneesai et al. 2023a). Keerati *et al.* used bulk reduced graphene oxide cement composites, displaying bipolar charge carriers with P-type to N-type switching at a temperature of 420K, and obtained an electrical conductivity of 37 S/cm (Maneesai et al. 2023b).

From 2020 onwards, thermoelectric materials have witnessed enormous development, including the inclusion of multiple phases of nanofillers to investigate the initial performance of cement composite paste/mortar, which showcases optimal performance in terms of compactness, mixing and strengthening of the interlayer interaction between nanofillers and the calcium silicate hydrate (C-S-H) matrix (Fan et al. 2025). Fu *et al.* found that incorporating graphene oxide into cement-based materials provides nucleation sites for cement hydration and reacts with ions released during hydration, exerting a catalytic effect on the hydration process (Fu et al. 2023). Partial oxidation can alter the electronic characteristics of cement-based materials, as evident in the incorporation of SWCNT, resulting in an electrical conductivity of approximately 1369 S/cm compared to approximately 283 S/cm for untreated materials (Stando et al. 2022). Adhesion mechanisms between (C-S-H) and fillers are directly related to the affinity of the filler's surface towards ions in the pore structure of cement paste. Filler surfaces and calcium ions adhere due to acid–base interactions, whereas in the case of silica, ion–ion correlation forces support adhesion. (Ouyang et al. 2017). In graphene and functionalized graphene-incorporated cement composites, early-age hydration kinetics are accelerated,

whereas only carbonyl graphene enhances the later-age hydration kinetics (Aadithya et al. 2024). The etching of expanded graphite (EG) enhances the connectivity of the expanded graphite conductive network of cement composites, resulting in a remarkable electrical conductivity of 7.43S/cm (Wang et al. 2025). Wei *et al.* structurally regulated the graphitisation degree of expanded graphite via acid treatment, thereby increasing electrical conductivity (Wei et al. 2024). It is now evident that the inclusion of conductive fillers and fibres at the nano/micro/macro levels develops conductive networks in the cement matrix (Bishnoi et al. 2025). Carbon-derived conductive fillers, such as graphene, carbon nanotubes (CNT), and carbon fibres, must be properly mixed and ground to prevent agglomeration and self-aggregation. Due to immiscibility, graphene-graphene species try not to mix with water-water species in the cement composite matrix.

The micro-filler can easily fill pores in the cement matrix, and percolation is observed at low dosage (**Figure S1, Supporting Information**). Materials can be categorised into three zones according to their electrical conductivity. An insulation zone, where very few conductive elements, like percolated ionic water or trapped isolated electrons/conductive species are found. They can exhibit very limited electrical conductivity, as in the case of pure cement paste, which shows very little electrical conductivity due to trapped ionic water (Frąc et al. 2024). When conductive fillers are introduced, if there is enough conductive material content to reach the percolation threshold, that is called the percolation zone. In the conductive zone, optimal conductive material content is reached, and high-order electrical conductivity is obtained, as in the case of conductors (**Figure S2, Supporting Information**). Electron transport in the composite is assisted by tunnelling across narrow gaps between dispersed nanofillers (**Figure S3, Supporting Information**). Continuous conductive networks are required for smooth conductivity. hopping and tunnelling, optimal percolation and a large area of filler support this.

Candle soot is an easily available household waste material for generating candle soot-based carbon nanoparticles (Speight 2011; Mulay et al. 2019). Flame shape and height play an important role in the generation of high-quality, conductive carbon nanoparticles(Hamins et al. 2005; Su et al. 2011; Sunderland et al. 2011). The candle flame's highest temperature, about 1980 K, occurs near the flame edge, indicating vigorous reactions that produce high-quality, smaller, chemically active soot particles (Thomsen et al. 2017; Zheng et al. 2019). Candle soot carbon undergoes functional transformations, making it a promising functional material, as validated by HR-TEM, XRD, and Raman analysis, showing the dominance of sp^2-bonded graphitic carbon hybridisation(Anil D. Pathak 2022)(Singh and Pradhan 2025). Candle soot

and its derivatives contain a high carbon content, making them suitable agents for creating conductive pathways for electron conduction(Singh et al. 2018).

In this study, we explored candle soot as an alternative carbon nanomaterial and developed and utilised candle soot-based carbon nanoparticles (CNP) as a conductive material. Previous studies have primarily focused on expansive nanomaterials such as graphene and carbon nanotubes. The use of candle soot remains limited in cementitious systems. The work demonstrates the feasibility of utilising candle soot-based carbon nanoparticles (CNP) and compares their effectiveness as conductive fillers in a cement composite system with those of the commercially available super-grade graphene and multiwall carbon nanotubes. The study provides insight into the effect of filler dosage on material performance while maintaining a constant water-to-cement ratio. The findings contribute to the development of such materials for a wide range of charge storage applications.

Materials Taken and Experimental Procedure

2.1 Raw Materials

Ordinary Portland cement (OPC) 43 Grade (Ultratech, India), columniform white paraffin wax candles, steel plate (soot collection), steel bowl to place the broken molten candle wax, spatula, airtight glassware, centrifuge tube, were purchased from the local supplier (Pilani, Rajasthan, India), and isopropyl alcohol (C_3H_8O, 99.5% is used as received. Super grade graphene (SGG) (>99.0%) and MWCNT (>99.0%) were purchased from BTCORP Generique Nano Pvt. Ltd, Bangalore, India. The physical and chemical properties of OPC, MWCNT and SGG are presented in **Table S1, Table S2 and Table S3 in the Supporting Information**.

2.2 Candle soot to carbon nano particle (CNP)

2.2.1 Collection, preparation, and synthesis of carbon nano particles (CNP):

An iron tripod with a circular top ring holds the stainless-steel plate, which collects the soot (**Figure 1a**). Candle wax is collected into the steel bowl. A 2 mm-thick, 30mm-long cotton wick is inserted to cast a candle and placed into this bowl.

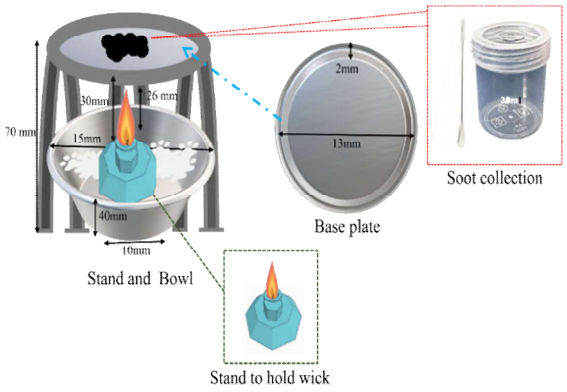


Figure 1a. Preparation for soot collection

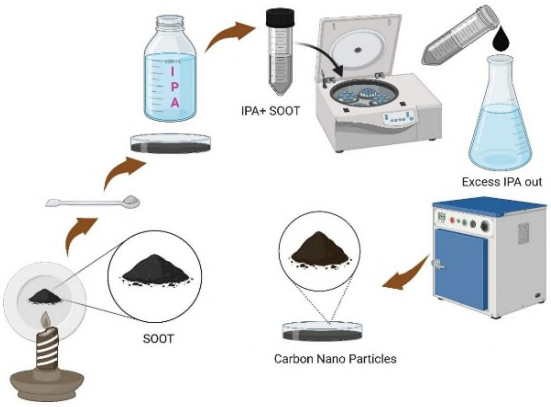


Figure 1b. Collection and synthesis of candle soot to CNP

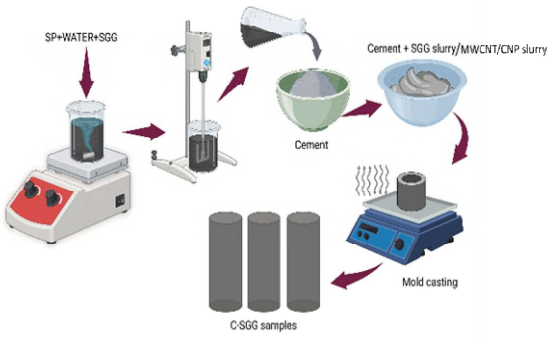


Figure 1c. Preparation process of cement conductive filler composite samples

During candle combustion, a steel plate is placed directly above the candle wax setup (bowl with candle wax, wick, and metal stand) so that the wick flame tip touches it. The candle wick height is adjusted through a homemade metal stand. During the soot collection phase, the soot from the base plate is gently scraped into an airtight container using a spatula. Typically, 50 g of soot is divided into six 50-ml centrifuge tubes. The soot is repeatedly washed with isopropanol, giving it a black-ink appearance. The mixture is transferred to a centrifuge machine (Compufuge, Remi) and operated at 10,000 rpm for 30 minutes. The final product settles, leaving the rinsed IPA alone and thereby mixing the unburnt hydrocarbons and impurities with the IPA. Finally, decanting the excessive IPA helps to separate the synthesised soot. The residue is placed in a crucible and heated for 2 hours at 100°C. The final dried leftover product is carbon nanomaterials (CNP) (**Figure 1b**).

2.2.2 Physicochemical characterisation of candle-soot

The candle soot and the prepared carbon nanoparticles (CNP) are examined using morphological and spectroscopic techniques. Morphological analysis and energy-dispersive X-ray spectroscopy (EDS) were performed using scanning electron microscopy (FE-SEM Apreo LoVac, FEI). Transmission electron microscopy (TEM) (JOEL, JEM-1400), operating at 120 kV, was used to determine the particle core diameter and lattice. Soot was mixed in IPA (1mg/mL), and a drop was placed onto a 200-mesh holey carbon-coated copper grid. Analysis of micrographs was performed using ImageJ software at low and high resolutions. Powder X-ray diffraction (XRD) measurements were performed using an Ultima IV (Rigaku) diffractometer with Cu Kα radiation (λ = 1.5406 Å), operated at 40 kV and 30 mA, at a scan rate of 2° min^{-1} over a 2θ range of 10°–60°. X-ray Photoelectron Spectroscopy (XPS) (Thermo Fisher Scientific, K-Alpha) was used to analyze the surface chemistry. Fourier transform infrared spectroscopy (FTIR) Alpha Bruker) spectra were recorded by the KBr pellet method with a Perkin-Elmer spectroscope. Raman spectra (HORIBA LABRAM) of the samples were analyzed using an excitation wavelength of 633 nm. Raman spectroscopy and X-ray diffraction (XRD) were used to investigate graphitisation and crystallinity of different planes, where the degree of graphitisation was evaluated using the Raman intensity ratio (I_D/I_G). Brunauer-Emmett-Teller (BET) analysis was performed using a SORP mini-II (Microtrac BEL) to determine the specific surface area at 120 °C for 8 hours under nitrogen. From the adsorption branch of the obtained isotherm, pore size distribution can be found using the Barrett-Joyner-Halenda (BJH) method. The thermogravimetric analysis (TGA) (Shimadzu) analysis of the soot and nanoparticles was performed by placing the samples in the sampler bowl. The wettability of soot collected from the flame zones was evaluated using the sessile drop method on a contact angle goniometer (Ossila), with analysis performed using KRUSS ADVANCE software. Molecular size analysis and zeta potential for charge, stability and behaviour of colloidal nanoparticles were studied using the Litesizer 500 (Anton Paar). Laser Doppler velocimetry helps determine the Zeta potential, an indicator of colloidal solution stability. Solid-state ^{13}C NMR spectroscopy (JEOL JNM-ECZL400G, 400 MHz, FT) was conducted on 50 mg of soot to investigate its surface structure.

Specimen fabrication

The cement composite samples were prepared using OPC and three different fillers (SGG, MWCNT, and CNP). They were added individually by weight of dry cement (**Table 1**). It is then ground to remove agglomerates and lumps, resulting in an evenly dispersed mix. A constant water-to-cement ratio(w/c) of 0.40 was maintained on a dry-weight basis. The

nanomaterials were treated as fillers/additives and were not considered in the w/c calculations, since they do not contribute to the hydration process of cement.

The wet-mixing method was employed in this study. Customised 3D-printed moulds were used to cast cylindrical samples measuring 15 mm in diameter and 30 mm in height to prepare the cement–nanomaterial matrix (**Figure 1c**). The samples were demoulded after 24 hours and subsequently air-dried for 7 days to remove residual moisture. After drying, the specimens were cut to obtain final samples with a diameter of 15 mm and a thickness of 3 mm. The surfaces of the prepared samples were then polished using 800-grit and 1200-grit emery sandpaper to ensure smoothness. The nomenclature used for the samples, along with the mix proportion, is shown in **Table 1.**

Table 1. Mix Proportions details

Sl. No	Mix ID	Cement (g)	Filler Name	Filler Content (% by wt. of cement)	Water (g)
1	CEM	100	--	0%	40g
2	CSGG1	100	Super-grade graphene	1%	40g
3	CSGG2	100	Super-grade graphene	2%	40g
4	CSGG3	100	Super-grade graphene	3%	40g
5	CSGG4	100	Super-grade graphene	4%	40g
6	CSGG5	100	Super-grade graphene	5%	40g
7	CMWCNT5	100	MWCNT	5%	40g
8	CMWCNT7.5	100	MWCNT	7.5%	40g
9	CMWCNT10	100	MWCNT	10%	40g
10	CMWCNT12.5	100	MWCNT	12.5%	40g
11	CMWCNT15	100	MWCNT	15%	40g
12	CCNP5	100	Carbon nanoparticle	5%	40g
13	CCNP7.5	100	Carbon nanoparticle	7.5%	40g
14	CCNP10	100	Carbon nanoparticle	10%	40g
15	CCNP12.5	100	Carbon nanoparticle	12.5%	40g
16	CCNP15	100	Carbon nanoparticle	15%	40g

2.3 (Physicochemical and electrical characterisation of cement composites Microscopic and Spectroscopic examination

The tablet samples were dried at 60 °C for 24 h, followed by gold coating using a sputter coater. The coated specimens were examined using a field-emission scanning electron microscope (FE-SEM) operated at 10 kV. FE-SEM analysis was used to investigate the surface

morphology, dispersion of carbon nanotubes, and nano-interfacial characteristics between the fillers and the cement matrix. The percolation threshold was qualitatively inferred from the presence of agglomeration or re-agglomeration, observed as localised nanomaterial clusters distributed across the matrix.

X-ray diffraction (XRD) was employed to examine crystal structure evolution and phase composition, and to indirectly assess filler distribution and the formation of a conductive network. Raman spectroscopy was utilised to evaluate the degree of graphitisation (via I_D/I_G) and to identify structural and chemical modifications within the cement matrix.

Electrical Conductivity Measurement

Electrical measurements were performed using a Keithley 4200A Semiconductor Parameter Analyser (Convergent Technologies), configured in a four-probe geometry to ensure uniform electrical contact with the cement composite tablet (**Figure S4 Supporting Information**). In this configuration, two source measurement units (SMUs) were used to source current, while the remaining two SMUs measured the corresponding voltage drop across the sample (**Figure S5 Supporting Information**).

Electrical resistivity was determined using the Clarius software environment. Temperature-dependent measurements were conducted using a proportional–integral–derivative (PID) controller, maintaining the sample temperature between 30 °C and 85 °C. A low current was applied in linear-sweep mode, ranging from 0 to 1 mA with a step size of 10 µA, and a voltage compliance limit of 20 V.

3. Results and Discussion

3.1 Physicochemical analysis of Carbon Nanoparticles

FESEM confirms that the produced CNP are spherical, with a rough, textured surface and shorter, looser carbon chains. Similar structures are seen in the work of Pathak and Hao (Anil D. Pathak 2022; Hao et al. 2022), as shown in **Figure 2(a-d)**. The carbon presence is 90%, as indicated by the electron map spectrum sum in **Figure 2(e-g**). The EDS layered image indicates the presence of other elements, including oxygen (6%), sulphur, silicon, and potassium, in very small traces. A similar composition is also reported by Das et al (Das et al. 2017).

HR-TEM reveals sharp, spherical fringes, indicating a high defect density(Xiao et al. 2018), exhibiting concentric nano-onion rings (Anil D. Pathak 2022), with a maximum particle size of 30nm, **Figure 2(h-j).** The presence of clear lattice fringes corresponding to the (002)

crystallographic plane confirms the graphitic basal plane structure of the material (Anil D. Pathak 2022). ImageJ software and fast Fourier transform (FFT) analysis yield a graphitic layer spacing of d(002) as (0.35nm), indicating the dominance of turbostratic graphitic domains. The stacking of the graphene layers is highly disordered; similar structures are also reported by Muley et al. (Mulay et al. 2019). The selected area electron diffraction (SAED) in **Figure 2(k)** shows fringes with sharp, thin concentric rings, indicating the presence of sp^2 hybridised carbon (Anil D. Pathak 2022)(Chauhan et al. 2025). Solid-state magic-angle spinning NMR of the C^{13} nucleus showed a sharp peak at 115 nm, indicating a dominance of sp^2 hybridisation **Figure 3(a)**. The aromatic/alkene range generally lies between 100 ppm and 160 ppm (Liu et al. 2007).

In the XRD spectrum, the (002) and (100) peaks show variation in the degree of graphitisation after treatment(Justin Raj et al. 2016). A prominent diffraction peak corresponding to the (002) plane, which is associated with the interlayer stacking of graphitic basal planes along the c-axis. In addition, a weaker peak corresponding to the (100) plane is observed, indicating in-plane ordering of sp^2-bonded carbon atoms (Justin Raj et al. 2016; Mulay et al. 2019; Anil D. Pathak 2022). The presence of these characteristics confirms the material's graphitic crystalline structure. A broad peak indicates an amorphous nature as seen in **Figure 3(b)**.

Thermogravimetric examination indicates good stability with minimal mass loss, as also reported in candle soot by Thota et al. (Thota et al. 2023), **Figure 3(c)**. Raman spectra indicate a change in structure, accompanied by enhanced electrical conductivity, as evidenced by a change in the I_D/I_G ratio from 1.19 to 1.02 after treatment [55] **Figure 3(d).** The XPS survey spectrum indicates that the sample is predominantly composed of carbon atoms (approximately 90%), with a smaller proportion of oxygen (around 10%), as shown in **Figure 3(e).** XPS examination and the map-sum spectra of carbon and oxygen reveal variation and enrichment in hybridisation with an increased sp^2 area relative to sp^3, as shown in **Figure 3(f-g).** A Similar observation is reported by Pathak et al. after XPS examinations(Anil D. Pathak 2022). BET plot of CNP in **Figure 3(h-i)** indicates an improved specific surface area and denser pore structure(Justin Raj et al. 2016). The average pore radius of candle soot is 27 nm, for CNP it is 16 nm (**Table S4, Supporting Information).** The incremental pore volume and incremental pore area are improved (**Figure S6(a-b), Supporting Information).** A Similar observation is seen after soot treatment in the work of Qahtan et al. (Qahtan et al. 2017). The cumulative pore volume and cumulative pore area of CNP (**Figure S6(c-d), Supporting Information**) are

reduced, which is a good indicator of enhanced electrical conductivity; a similar observation is reported by CJ Raj et al.(Justin Raj et al. 2016).

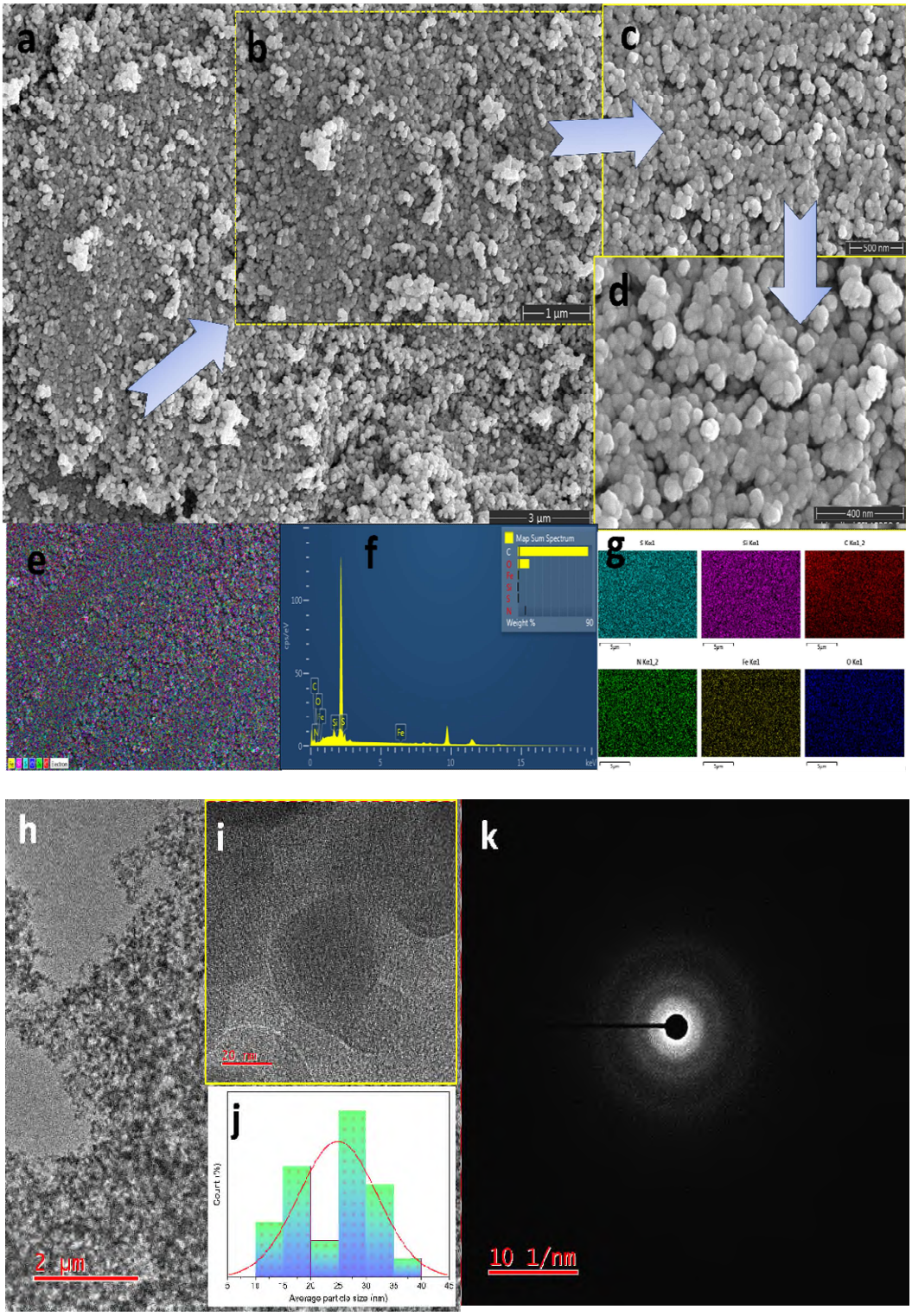


Figure 2: FE SEM of CNP: (a-d) at lower to higher resolution, (e) EDS layered image. (f) Map sum spectrum, (g) Elemental map. HR-TEM of CNP: (h) Low resolution, (i) High resolution, (j) Particle size distribution, and (k) SAED image of Concentric Fringes at $d_{(002)}$

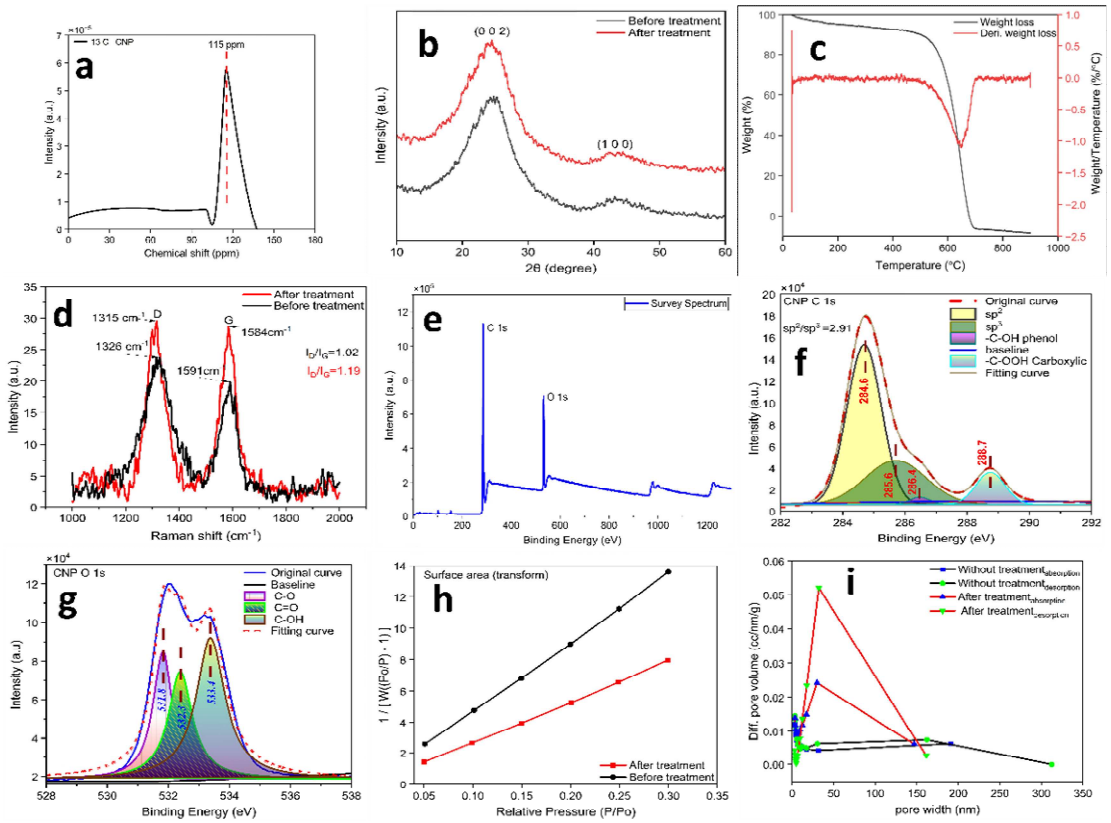


Figure 3. CNP (a) 13-C NMR (b) XRD (c) TGA and DTGA (d) Raman shift (e) XPS survey spectrum (f) XPS C 1s (g) XPS O 1s (h)BET Surface area and (i) BET volume variation.

3.2 Physicochemical analysis of cement composites

In FESEM micrographs, cement hydration products and the densified matrix are visible in **Figure 4(a-c)**. The electron map image **Figure 4(d)** and EDS mapping **Figure 4(e)** with elemental composition of cement, indicating the presence of calcium, silicon, and other species **Figure 4(f)**. Once the nanofillers (CNP, MWCNT, and SGG) are mixed separately according to the designed proportions and ground, agglomeration is reduced, resulting in a uniform-coloured powder. The cement-CNP hydration products, such as C-S-H gel and ettringite in **Figure 4(g-h)**, are well-formed. In the cement-MWCNT mix, thread-like formations and cement hydration products, as shown in **Figure 4(i-j),** are visible(An et al. 2024)(Wei et al. 2021b), whereas in the cement -super grade graphene mix, as shown in **Figure 4(k-l)**, bulky, paper-like structures, C-S-H gel, ettringite, and portlandite structures are observed(Wang et al. 2025). The electron map images, EDS, and elemental composition of cement-SGG mix support a uniform distribution of carbon in the Ca-Si regions and in the hydration products, with no agglomerates, indicating a homogeneous dispersion of graphene sheets, as shown in **Figure S7(a-c), Supporting Information.** The EDS of cement-CNP mix indicates a uniform

distribution of carbon nanoparticles throughout the cement matrix, with fine carbon particles filling pores, and greater densification, as compared to SGG/MWCNT, as shown in **Figure S7(d-f), Supporting Information.** The EDS mapping of the cement-MWCNT mix shows localised but interconnected carbon-rich regions, with evidence of network formation and carbon bridging across hydration phases, as shown in **Figure S7(g-i), Supporting Information**.

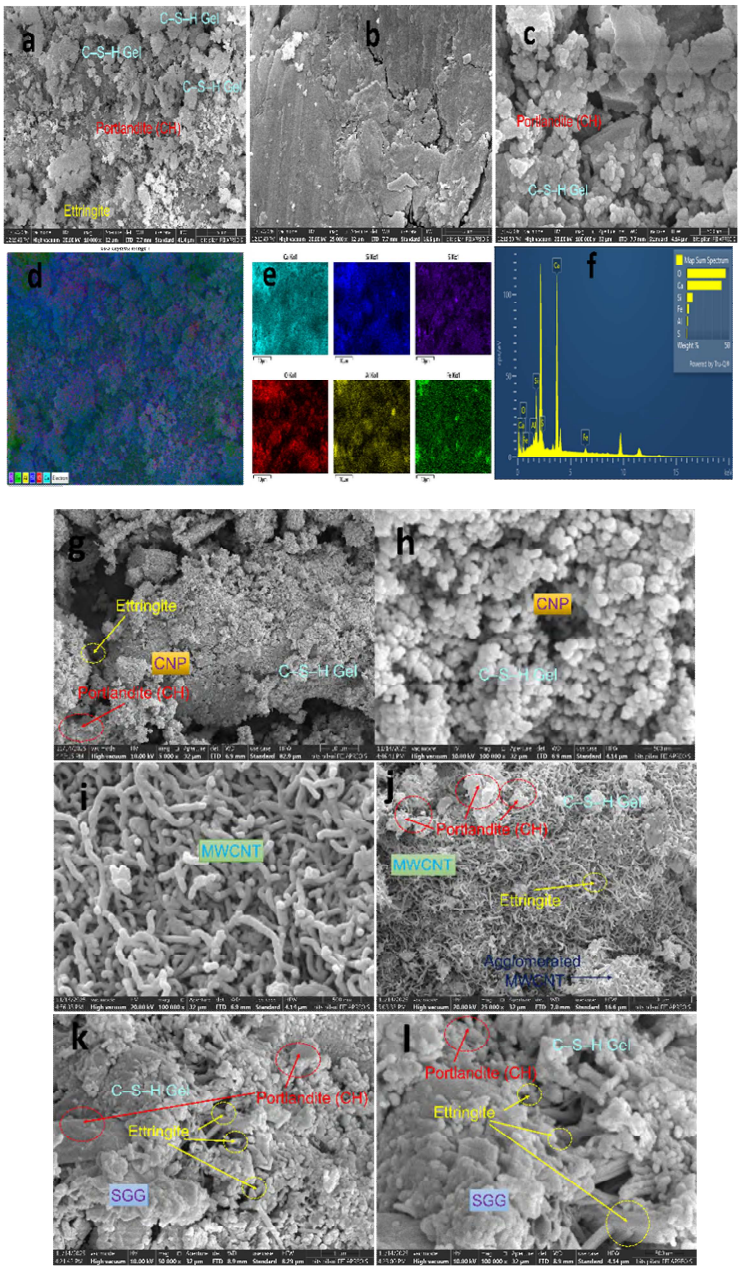


Figure 4: Cement control mix: (a-c) micrographs, (d)Electron image, (e) EDS mapping and (f) elemental composition. Micrographs of cement-CNP mix (g-h), cement-MWCNT mix (i-j) and cement-SGG mix (k-l).

3.2 X-Ray Diffraction analysis:

XRD examination of the cement control mix, as shown in **Figure S8(g), Supporting Information,** indicates the formation of hydration products by detecting the crystalline phases present in the cement matrix. The portlandite peak (102) is observed at 43°, and the calcite peak (202) is seen at 64°. In carbon nanoparticles (CNP), **Figure S8(f), Supporting Information**, a broad peak is observed at 24°, further strengthening the amorphous nature of CNP(Anil D. Pathak 2022)(Mulay et al. 2019) with disordered carbon. In MWCNT, **Figure S8(e), Supporting Information**, the (002) peak of CNT stacking is observed at 26°, and a broader graphitic peak (100) is seen at 44°(An et al. 2024). In the super-grade graphene, **Figure S8(d), Supporting Information**, the graphitic (100) peak is observed at 44°, whereas the graphene interlayering basal plane (002) is observed as a broader peak at 24°. In the cement–CNP composite in **Figure S8(c), Supporting Information**, the presence of the in-plane carbon peak (100) at 44° indicates uniform dispersion of the nanomaterial. In contrast, the control mix exhibits a portlandite peak (102) at 43° and a calcite peak (002) at 64°. Notably, in the composite, the peak near 64° corresponds to carbon-related features rather than calcite, suggesting the formation of carbon-rich hydration products and distinguishing it clearly from the control sample. In the cement–MWCNT composite in **Figure S8(b), Supporting Information**, the CNT (100) peak is observed at approximately 43°. In the MWCNT sample, this peak shifts to around 44°, indicating an enhanced CNT–cement interface and the formation of more pronounced carbon-stacked hydration products. Additionally, the calcite (002) peak is observed at 65° (Wei et al. 2021b). In the cement–SGG composite in **Figure S8(a), Supporting Information**, a graphitic (100) peak is observed at 44°, consistent with the peak position in the SGG material itself. This correspondence suggests the incorporation of graphene within the cement matrix. The peak characteristics further indicate a well-dispersed graphene network, contributing to an extended conductive structure. After hydration, a calcite (202) peak appears at 64°, supporting the uniform densification of the calcium–silicate phase in the cement–SGG composite.

3.3 Raman analysis

Raman spectral analysis (**Figure S9(g), Supporting Information)** shows that hydration products in the control cement mix can be identified by characteristic vibrational peaks at different hydration stages. OH^- bending at 272 cm^{-1} and interlayer H_2O at 350 cm^{-1}, along with a broad hydration band in the range of 430–460 cm^{-1}. The Si–O stretching vibration appears at

540 cm^{-1}, while portlandite (CH) is identified at 680 cm^{-1}. A carbonate band is observed at 875 cm^{-1}, and the sulfate peak associated with ettringite occurs at 1000 cm^{-1}. Further carbonate stretching is evident at 1085 cm^{-1}, and an additional portlandite peak is observed at 2528 cm^{-1} (Kirkpatrick et al. 1997; Potgieter-Vermaak et al. 2006; Liu and Sun 2016; Polavaram and Garg 2021). The distortion and graphitisation bands for CNP, shown in **Figure S9(f), Supporting Information,** are seen at 1315 cm^{-1} and 1584 cm^{-1}, with an I_D/I_G ratio of 1.02. The peaks are broader, indicating an amorphous nature (Justin Raj et al. 2016; Mulay et al. 2019; Anil D. Pathak 2022). For the MWCNT, as shown in **Figure S9(e), Supporting Information**, the D band and G band are observed at 1339 cm^{-1} and 1570 cm^{-1}, respectively. The 2D band is also visible at 2673 cm^{-1}. The peaks are sharper than those of CNP, indicative of its greater stacking behaviour (Article et al. 2020). The I_D/I_G ratio found is 0.86. For the super-grade graphene shown in **Figure S9(d), Supporting Information**, the D and G bands are observed at 1330 cm^{-1} and 1570 cm^{-1}, with a broader 2D peak between 2680 and 2700 cm^{-1}. The I_D/I_G ratio is 0.85. When these nanofillers are mixed into the cement, the bands are shifted, and peaks are obtained at different locations, indicating the presence of the cement nanofiller (Azeem and Saleem 2022). As in the cement-CNP composite, **Figure S9(c), Supporting Information**, the gap between the D and G bands increased with a lower peak height, indicating a homogenised mixing of the CNP nanofiller (Anil D. Pathak 2022; Yaghobian and Whittleston 2022). In the case of the cement-MWCNT composite, **Figure S9(b), Supporting Information**, the peaks are broader for the D and G bands, and the peak heights are also reduced (Azeem and Saleem 2022). In the case of cement-SGG composite, **Figure S9(a), Supporting Information**, C-S-H formation is observed at 278 cm^{-1} and 1087 cm^{-1}, and the calcite peak is observed at 715 cm^{-1}.

Electrical Conductivity Measurement of SGG, MWCNT, and CNP Cement Composites

Each sample type is prepared in three independent batches, with three readings per batch for electrical conductivity measurement. The electrical conductivity of the cement control mix, as shown in **Figure 5(d)** is 3.32×10^{-8} S/cm at 30 °C. With an increase in temperature to 45°C, the electrical conductivity is observed to be 3.35×10^{-8} S/cm, further increase in the temperature from 45°C to 85 ℃ made a very slight increase in electrical conductivity, an increment of up to 3.38×10^{-8} S/cm. Thus, limited electrical conductivity is observed, which may be attributed to the presence of pore water and ionic conductivity in the cement sample.

The addition of MWCNTs significantly enhanced the electrical conductivity of cement-MWCNT composites in **Figure 5(c)**. At a 5% MWCNT concentration, the electrical

conductivity reached 0.05 S/cm at 30 °C and remained constant at 85 °C. With a 7.5% dosage, the electrical conductivity increased to 0.075 S/cm at 30 °C and increased slightly with increasing temperature. At this dose, the highest electrical conductivity was reached at 0.085 S/cm at 85 °C. When the dose is further increased to 10%, the electrical conductivity at 30 °C is 0.10 S/cm and remains constant, showing no variation with increasing temperature up to 85 °C. With an increment in dose to 12.5 % at 30 °C, the electrical conductivity jumped to 0.19 S/cm. In this mix, when the temperature is increased to 85 °C, the electrical conductivity falls to 0.16 S/cm. Increasing the dosage to 15% resulted in the highest electrical conductivity of 0.26 S/cm at 30 °C, due to the formation of a dense, well-connected MWCNT network, as evident from **FESEM** in **Figure 4(i-j)**. An increase in temperature disrupted conductivity, with slight increases and decreases, reaching a maximum electrical conductivity of 0.28 S/cm at 60 °C. Increasing the temperature to 85 °C reduced the electrical conductivity to 0.25 S/cm. The higher aspect ratio and bridging capability of MWCNTs facilitated efficient electron transport and increased conductivity with increasing filler content (Ding et al. 2025).

When the Cement-CNP composite sample in **Figure 5(b)** is subjected to electrical conductivity measurements, the electrical conductivity at a 5% CNP concentration is observed to be 0.03 S/cm at 30 ºC. At 50 °C, the electrical conductivity reduced marginally to 0.028 S/cm. At 55 ºC, the electrical conductivity is 0.031 S/cm. With a further increase in temperature from 60°C to 85°C, electrical conductivity increased to a maximum of 0.033 S/cm at 85 ºC. Lower dosage is effective in percolated conductive networks. However, a further increase in dosage to 7.5% results in an electrical conductivity of 0.025 S/cm at 30 °C. At temperatures up to 85 °C, electrical conductivity decreases to 0.023 S/cm. But when the CNP dose is increased to 10%, electrical conductivity jumps to 0.027 S/cm at 30 °C, and increasing the temperature lowers it to 0.026 S/cm at 50°C. However, at 85°C, the conductivity fluctuates, reaching 0.027 S/cm. Further increasing the dose to 12.5% lowered the electrical conductivity to 0.012 S/cm, and the temperature increase did not result in any additional increment. The maximum dose of 15 % CNP increased electrical conductivity to 0.015 S/cm at 30 ºC. When the temperature increased to 85 °C, the conductivity increased to 0.017 S/cm. The fluctuation in electrical conductivity is likely due to CNP particle agglomeration at higher doses, as seen in FESEM micrographs in **Figure 4(g-h).** Increased porosity, cross-linking, and nanoparticle chain and network breakage disrupt the CNP cement matrix.

In cement-SGG composite **Figure 5(a)**, the incorporation of super-grade graphene marginally enhances the electrical conductivity of the cement composites in comparison to the cement-

CNP composites. At a 1% SGG concentration, the conductivity was 0.01 S/cm at 30°C. As the temperature increased to 65°C, electrical conductivity increased to 0.02 S/cm; upon further increasing the temperature to 85 °C, it decreased to 0.015 S/cm. At an SGG dosage of 2%, the electrical conductivity at 30°C is 0.019 S/cm. With increasing temperature, the conductivity rises to 0.021 S/cm at 35°C and further increases to 0.039 S/cm at 40°C. At 45 °C, the electrical conductivity is 0.045 S/cm, and at 50°C it increases to 0.052 S/cm. A further rise in temperature to 55 °C results in a conductivity of 0.060 S/cm. At 65°C and 75°C, the electrical conductivity reaches 0.072 S/cm, the highest value observed for the 2% dosage. However, with a further increase in temperature to 85°C, the electrical conductivity decreases slightly and stabilises at 0.065 S/cm.

This 2% content of SGG strongly suggests a percolation threshold with strongly conductive networks and minimal agglomeration, and a dense matrix of graphene-cement hydration products with uniform distribution. When the dose is increased to 3%, the electrical conductivity falls to 0.019 S/cm at 30 °C. This trend is consistent with increased temperature up to 55 °C, and a further increase to 85 °C steadily lowered electrical conductivity to 0.015 S/cm. When 4% SGG is incorporated, the electrical conductivity is 0.021 S/cm at 30 °C; at 35 °C, it jumps to 0.026 S/cm and increases sharply to 0.048 S/cm at 75 °C. At 85 °C, electrical conductivity reached a maximum of 0.055 S/cm, indicating the formation of effective percolation cement-SGG networks. At 5% dosage and 30°C, the electrical conductivity is 0.018 S/cm, and there is no significant increase in electrical conductivity with increasing temperature. These observations suggest that the optimum SGG content is 2%, beyond which electrical conductivity diminishes due to excessive filler-induced aggregation.

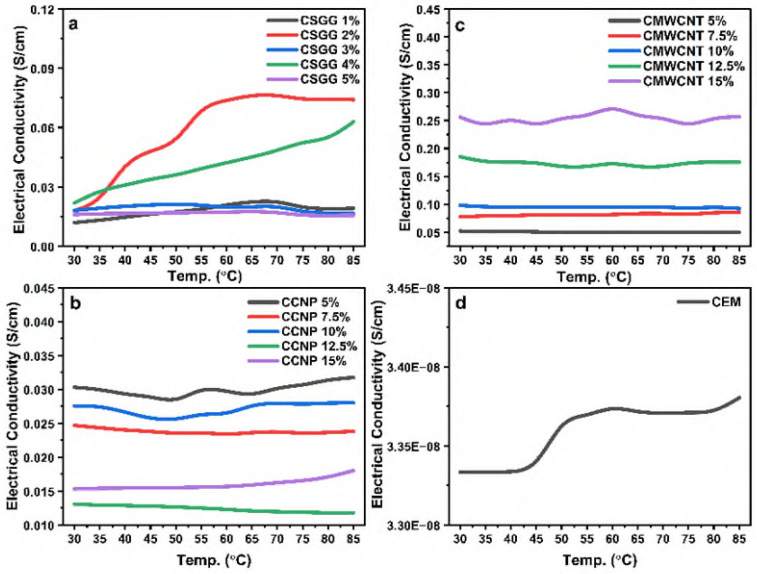


Figure 5: Electrical conductivity of: (a) Cement-SGG composite, (b) Cement-CNP Composite, (c) Cement-MWCNT composite, (d) Cement control mix.

434

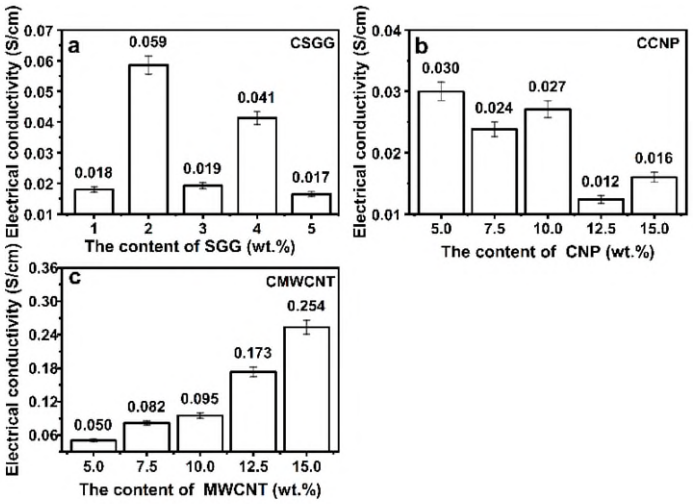


Figure 6: Electrical conductivity vs filler per cent (a) CSGG, (b) CCNP, (c) CMWCNT

435

436 Percolation threshold and tunnelling phenomena are observed in cement nanofiller composites.
437 For the cement-SGG composite in **Figure 6(a),** at 1% dosage, there is a significant increase in
438 conductive networks compared to the cement control mix. At 2%, the percolation threshold
439 appears to be reached, as evidenced by the electrical conductivity and FESEM results. When
440 the dose per cent is further increased to 3%, there may be an overlapping of continuous
441 networks; however, the dose at 4% strongly suggests the percolation threshold, and at the

highest dose of 5%, signals agglomeration. Moreover, the largest electrical conductivity jump is observed at 2% dosage due to the formation of longer conductive networks.

For the cement-CNP composite in **Figure 6(b)** at a 5% CNP filler dose, significant electrical conductivity is observed, strongly suggesting a percolation threshold and smaller CNP forms form continuous networks in the CCNP composite. Increasing the dosage to 7.5% slightly reduced the electrical conductivity, although the change was not significant. This behaviour may be attributed to the rearrangement of smaller CNP networks, possibly due to layer formation or particle overlap. A further increase in dosage to 10% and beyond led to agglomeration, which became more pronounced up to 15%.

The cement MWCNT composite electrical conductivity in **Figure 6(c)** suggests a higher electrical conductivity as compared to cement-SGG and cement-CNP composites. A higher aspect ratio of MWCNTs may be a factor in reduced agglomeration and improved dispersion, with minimal disruption of conductive pathways. The percolation threshold is reached at 15%, and at this stage, larger agglomerates are seen in the FESEM analysis.

4. CONCLUSIONS

Candle soot, a household waste product, can be converted into a sustainable carbon-based nanomaterial. The process of making CNP is simple and efficient. Cement composites develop a conductive network upon nanofiller incorporation, allowing current to flow through electronic and ionic conduction through trapped pore water. When pore water is reduced over time, only electronic conductance, enabled by nanofillers, remains. When these conductive networks are continuous, they allow current to flow, making the cement composite conductive. Nanofiller interaction occurs through physical contact, electron tunnelling, and interfacial bonding within the cement matrix. Temperature can enhance electron mobility and reduce contact resistance, thereby improving conductivity. This behaviour is evident when cement–nanofiller composites are subjected to a gradual increase in temperature, initially promoting the alignment and activation of conductive pathways, and eventually leading to percolation, which may occur through electron tunnelling. Cement-CNP samples exhibited electrical conductivity due to the shorter carbon chain of the spherical nanoparticles. However, as higher doses are administered, electrical conductivity decreases even though microstructural and spectroscopic examinations indicate a uniform distribution of nanofillers.

When the Cement-CNP samples were analysed, the maximum electrical conductivity was observed at 5% CNP dosage, beyond which conductivity decreased, likely due to

agglomeration and disruption of conductive pathways. The incorporation of CNP increased electrical conductivity by approximately 6 to 7 orders of magnitude compared to plain cement paste. Increasing temperature increases the electrical conductivity of CNP-based cement composites.

Plain cement paste exhibited a low electrical conductivity of 3.35×10^{-8} S/cm. The incorporation of MWCNTs into cement resulted in a substantial increase in conductivity, reaching 0.25 S/cm at 15% dosage. The continuous increase in conductivity with MWCNT content indicates effective formation of conductive pathways due to the high aspect ratio of nanotubes within the cement matrix. Temperature-dependent measurement showed only minor variations in conductivity, suggesting that filler-induced percolation governs the electrical behaviour of the cement-MWCNT composites.

The extremely low electrical conductivity of cement is enhanced by the incorporation of SGG. At a lower super-grade graphene dose (2%), electrical conductivity increased with temperature, reaching a maximum of 0.07 S/cm around 65ºC, indicating thermally activated charge transport, followed by a slight decrease at higher temperatures due to microstructural effects. At an intermediate dosage of 3%, the conductivity showed minimum temperature dependence, suggesting saturation of conductive pathways. A rapid increase in electrical conductivity with increasing temperature was observed at 4% SGG content. Further increasing the SGG content to 5% resulted in temperature-insensitive behaviour, likely due to agglomeration and network saturation. The inclusion of nanomaterials can create conductive paths and support the flow of electrical current. A percolation threshold is seen in the cement nanofiller composites. This suggests that carbon-based nanomaterials can enhance electrical conductivity compared to the cement control mix.

Acknowledgement

The authors express their gratitude to BITS Pilani, Pilani campus, for the fellowship, which supported their research endeavours and contributed to the successful execution of the study. We thank the Director of the Birla Institute of Technology & Science Pilani, Pilani campus, Rajasthan, for providing essential facilities that facilitated the research process. The authors also appreciate the Central Instrumentation Facility of the Birla Institute of Technology & Science- Pilani, Pilani campus and the Indian Institute of Technology, Delhi, for providing instrumental facilities crucial to the study.

Author Contributions

Thakur Ramjiram Singh: Writing – original draft, Data collection, experiment, figures and tables

Subhasis Pradhan: Funding acquisition, Conceptualization, Supervision, Writing – review & editing

Shiv Singh: Supervision, Writing – review & editing

Dheerendra Singh: Supervision, Writing – review & editing

Conflicts of interest: There is no conflict of interest among authors.

Data Availability: Most of the data is provided in the manuscript and ESI. If further required, it will be available upon request.

Declaration of generative AI and AI-assisted technologies in the writing process

During manuscript preparation, Grammarly was used to check grammar and enhance readability. The authors subsequently reviewed and edited the content as required and assume full responsibility for the published article.

References

Aadithya M, Sunil R, Gomosta S, et al (2024) Behavior of functionalized graphene in fresh and hydrated cement matrix: Role of carboxyl and amine functional group. Constr. Build. Mater. 450

Ahmad S, Abdul Mujeebu M, Farooqi MA (2019) Energy harvesting from pavements and roadways: A comprehensive review of technologies, materials, and challenges. Int J Energy Res 43:1974–2015. https://doi.org/10.1002/er.4350

An SH, Kim KY, Lee JU (2024) Reinforcement of Cement Nanocomposites through Optimization of Mixing Ratio between Carbon Nanotube and Polymer Dispersing Agent.

538 Polymers (Basel) 16:. https://doi.org/10.3390/polym16030428

539 Anil D. Pathak DP and CSS (2022) Graphitization induced structural transformation of candle
540 soot carbon into carbon nano-onion as a functional anode for metal-ion batteries. Mater
541 Adv 3610–3619. https://doi.org/10.1039/d2ma00042c

542 Article R, Du M, Jing H, et al (2020) Carbon nanomaterials enhanced cement-based
543 composites : advances and challenges. 115–135

544 Azeem M, Saleem MA (2022) A Raman Spectroscopic Study of Calcium Silicate Hydrate
545 (CSH) in the Cement Matrix with CNTs and Oxide Additives. J Spectrosc 2022:.
546 https://doi.org/10.1155/2022/2281477

547 Bishnoi P, Siwal SS, Singh N, et al (2025) Advanced Synthesis and Fabrication Strategies for
548 2D Mesoporous Carbon Materials in Energy Storage and Conversion. Adv Energy Sustain
549 Res. https://doi.org/10.1002/aesr.202500163

550 Cao H, Yao W, Qin J (2011) Seebeck effect in graphite-carbon fiber cement based composite.
551 In: Advanced Materials Research. Trans Tech Publications Ltd, pp 566–569

552 Carraro PA, Maragoni L, Paipetis AS, et al (2021) Prediction of the Seebeck coefficient of
553 thermoelectric unidirectional fibre-reinforced composites. Compos Part B Eng
554 223:109111. https://doi.org/10.1016/j.compositesb.2021.109111

555 Chauhan M, Budania Y, Modi A, et al (2025) Trifunctional Nature of Heteroatom (B, N, S,
556 O)-Doped Waste Diesel Soot: Turning Pollutants Into Potential Energy Catalysts for
557 HER, OER, and ORR. Carbon Neutralization 4:. https://doi.org/10.1002/cnl2.195

558 Das C, Chatterjee S, Kumaraswamy G, Krishnamoorthy K (2017) Elastic Compressible Energy
559 Storage Devices from Ice Templated Polymer Gels treated with Polyphenols. J Phys Chem
560 C 121:3270–3278. https://doi.org/10.1021/acs.jpcc.6b12822

561 Ding S, Dong S, Ashour A, Han B (2025) Development of sensing concrete: Principles,
562 properties and its applications. https://doi.org/10.1063/1.5128242

563 Duarte F, Ferreira A (2016) Energy harvesting on road pavements: State of the art. Proc Inst
564 Civ Eng Energy 169:79–90. https://doi.org/10.1680/jener.15.00005

565 Fan L, Zheng J, Wang H, et al (2025) Graphene oxide/carbon nanotubes harmonize to enhance
566 the initial hydration products and mechanical properties of cement mortar. Constr Build

Mater 474:141056. https://doi.org/10.1016/j.conbuildmat.2025.141056

Frąc M, Szołdra P, Teomete E, Pichór W (2024) Effect of internal moisture on the electric conductivity of cement composites with expanded graphite determined by impedance spectroscopy. Cem. Concr. Compos. 151

Fu Q, Wang Z, Xue Y, Niu D (2023) Catalysis and Regulation of Graphene Oxide on Hydration Properties and Microstructure of Cement-Based Materials. ACS Sustain Chem Eng 11:5626–5643. https://doi.org/10.1021/acssuschemeng.3c00109

Ghosh S, Harish S, Rocky KA, et al (2019) Graphene enhanced thermoelectric properties of cement based composites for building energy harvesting. Energy Build 202:1–7. https://doi.org/10.1016/j.enbuild.2019.109419

Hamins A, Bundy M, Dillon SE (2005) Characterization of candle flames. J Fire Prot Eng 15:265–285. https://doi.org/10.1177/1042391505053163

Hao L, Yangfan D, Qianyu Z, et al (2022) Construction of highly hydrophobic and fast endothermic surfaces using candle soot and nano-TiO2. 1046–1051

Jiang W, Yuan D, Xu S, et al (2017) Energy harvesting from asphalt pavement using thermoelectric technology. Appl Energy 205:941–950. https://doi.org/10.1016/j.apenergy.2017.08.091

Justin Raj C, Kim BC, Cho BB, et al (2016) Electrochemical supercapacitor behaviour of functionalized candle flame carbon soot. Bull Mater Sci 39:241–248. https://doi.org/10.1007/s12034-015-1113-7

Khasawneh MA (2025) Energy harvesting devices in pavement structures. Innov Infrastruct Solut 10:1–16. https://doi.org/10.1007/s41062-025-01996-x

Kirkpatrick RJ, Yarger JL, Mcmillan PF, Yu P (1997) Raman Spectroscopy of C-S-H , Tobermorite , and Jennite. 7355:

Li W, Du C, Liang L, Chen G (2026) Cement - Based Thermoelectric Materials , Devices and Applications. Springer Nature Singapore

Liu F, Sun Z (2016) Chemical mapping of cement pastes by using confocal Raman spectroscopy. Front Struct Civ Eng 10:168–173. https://doi.org/10.1007/s11709-015-0323-9

596 Liu H, Ye T, Mao C (2007) Fluorescent carbon nanoparticles derived from candle soot. Angew
597 Chemie - Int Ed 46:6473–6475. https://doi.org/10.1002/anie.200701271

598 Maneesai K, Khammahong S, Siripoom P, et al (2023a) Fabrication and thermoelectric
599 conversion of thermoelectric concrete brick with buried unileg N-type CaMnO3
600 thermoelectric module inside. Sci Rep 13:1–18. https://doi.org/10.1038/s41598-023-
601 28080-7

602 Maneesai K, Silakaew K, Khammahong S, et al (2023b) Temperature-dependent electrical
603 transport, Hall effect, and Seebeck properties of bulk chemically reduced graphene oxide
604 with bipolar charge carrier materials. AIP Adv 13:. https://doi.org/10.1063/5.0142476

605 Mendes JC, Barreto RR, de Paula ACB, et al (2019) On the relationship between morphology
606 and thermal conductivity of cement-based composites. Cem Concr Compos 104:103365.
607 https://doi.org/10.1016/j.cemconcomp.2019.103365

608 Mingqing S, Zhuoqiu L, Qizhao M, Darong S (1999) A study on thermal self-monitoring of
609 carbon fiber reinforced concrete. Cem Concr Res 29:769–771.
610 https://doi.org/10.1016/S0008-8846(99)00006-X

611 Moure A, Izquierdo Rodríguez MA, Rueda SH, et al (2016) Feasible integration in asphalt of
612 piezoelectric cymbals for vibration energy harvesting. Energy Convers Manag 112:246–
613 253. https://doi.org/10.1016/j.enconman.2016.01.030

614 Mulay MR, Chauhan A, Patel S, et al (2019) Candle soot: Journey from a pollutant to a
615 functional material. Carbon N Y 144:684–712.
616 https://doi.org/10.1016/j.carbon.2018.12.083

617 Ouyang X, Koleva DA, Ye G, van Breugel K (2017) Understanding the adhesion mechanisms
618 between C-S-H and fillers. Cem Concr Res 100:275–283.
619 https://doi.org/10.1016/j.cemconres.2017.07.006

620 Polavaram KC, Garg N (2021) Enabling phase quantification of anhydrous cements via Raman
621 imaging. Cem Concr Res 150:106592. https://doi.org/10.1016/j.cemconres.2021.106592

622 Potgieter-Vermaak SS, Potgieter JH, Van Grieken R (2006) The application of Raman
623 spectrometry to investigate and characterize cement, Part I: A review. Cem Concr Res
624 36:656–662. https://doi.org/10.1016/j.cemconres.2005.09.008

625 Qahtan TF, Gondal MA, Alade IO, Dastageer MA (2017) Fabrication of Water Jet Resistant

and Thermally Stable Superhydrophobic Surfaces by Spray Coating of Candle Soot Dispersion. Sci Rep 7:1–7. https://doi.org/10.1038/s41598-017-06753-4

Singh S, Bairagi PK, Verma N (2018) Candle soot-derived carbon nanoparticles: An inexpensive and efficient electrode for microbial fuel cells. Electrochim Acta 264:119–127. https://doi.org/10.1016/j.electacta.2018.01.110

Singh TR, Pradhan S (2025) Conductive Carbon Nanoparticle from Candle Soot: Waste to Wealth. In: Springer Proceedings in Materials. pp 433–441

Singh VP, Kumar M, Srivastava RS, Vaish R (2021) Thermoelectric energy harvesting using cement-based composites: a review. Mater Today Energy 21:100714. https://doi.org/10.1016/j.mtener.2021.100714

Speight JG (2011) Hydrocarbons from Petroleum

Stando G, Han S, Kumanek B, et al (2022) Tuning wettability and electrical conductivity of single-walled carbon nanotubes by the modified Hummers method. Sci Rep 12:1–13. https://doi.org/10.1038/s41598-022-08343-5

Su Z, Zhou W, Zhang Y (2011) New insight into the soot nanoparticles in a candle flame. Chem Commun 47:4700–4702. https://doi.org/10.1039/c0cc05785a

Sun M, Li Z, Mao Q SD (1998) Thermoelectric percolation phenomena in carbon fiber-reinforced concrete. Cem Concr Res 28:1707–1712

Sunderland PB, Quintiere JG, Tabaka GA, et al (2011) Analysis and measurement of candle flame shapes. Proc Combust Inst 33:2489–2496. https://doi.org/10.1016/j.proci.2010.06.095

Thomsen MC, Fuentes A, Demarco R, et al (2017) Soot measurements in candle flames. Exp Therm Fluid Sci 82:116–123. https://doi.org/10.1016/j.expthermflusci.2016.10.033

Thota K, Donthula K, Shekhar C, et al (2023) Candle soot nanoparticle embedded nanofibrous membrane for separation of miscible and immiscible oil/water mixtures. Polym Compos 44:4243–4251. https://doi.org/10.1002/pc.27394

Vizzari D, Gennesseaux E, Lavaud S, et al (2021) Pavement energy harvesting technologies: A critical review. RILEM Tech Lett 6:93–104. https://doi.org/10.21809/rilemtechlett.2021.131

655 Wang P, Wei J, Sheng L, et al (2025) Expanded Graphite/Cement Composites for Large-Scale
656 Energy Harvesting: Structural Control and Thermoelectric Properties. Langmuir
657 41:19088–19100. https://doi.org/10.1021/acs.langmuir.5c00897

658 Wei J, Fan Y, Zhao L, et al (2018a) Thermoelectric properties of carbon nanotube reinforced
659 cement-based composites fabricated by compression shear. Ceram Int 44:5829–5833.
660 https://doi.org/10.1016/j.ceramint.2018.01.074

661 Wei J, Nie Z, He G, et al (2014) Energy harvesting from solar irradiation in cities using the
662 thermoelectric behavior of carbon fiber reinforced cement composites. RSC Adv
663 4:48128–48134. https://doi.org/10.1039/c4ra07864k

664 Wei J, Sheng L, Lv E, et al (2024) Significant Improvement in Thermoelectric Properties of
665 Carbon-Reinforced Cementitious Composites Achieved by Regulating the Graphitization
666 Degree of Expanded Graphite. ACS Appl Mater Interfaces 16:35381–35389.
667 https://doi.org/10.1021/acsami.4c08270

668 Wei J, Wang Y, Li X, et al (2021a) Dramatically Improved Thermoelectric Properties by
669 Defect Engineering in Cement-Based Composites. ACS Appl Mater Interfaces 13:3919–
670 3929. https://doi.org/10.1021/acsami.0c18863

671 Wei J, Zhang M, Wang Y, et al (2021b) Synergistic optimization of thermoelectric
672 performance in cementitious composites by lithium carbonate and carbon nanotubes. Int
673 J Energy Res 45:2460–2473. https://doi.org/10.1002/er.5940

674 Wei J, Zhao L, Zhang Q, et al (2018b) Enhanced thermoelectric properties of cement-based
675 composites with expanded graphite for climate adaptation and large-scale energy
676 harvesting. Energy Build 159:66–74. https://doi.org/10.1016/j.enbuild.2017.10.032

677 Wen S, Chung DDL (2000) Seebeck effect in steel fiber reinforced cement. Cem Concr Res
678 30:661–664. https://doi.org/10.1016/S0008-8846(00)00205-2

679 Wen S, Chung DDL (2002) Thermoelectric behavior of carbon-cement composites [1]. Carbon
680 N Y 40:2495–2497. https://doi.org/10.1016/S0008-6223(02)00142-2

681 Xiao L, Zeng W, Liao G, et al (2018) Thermally and Chemically Stable Candle Soot
682 Superhydrophobic Surface with Excellent Self-Cleaning Properties in Air and Oil. ACS
683 Appl Nano Mater 1:1204–1211. https://doi.org/10.1021/acsanm.7b00363

684 Yaghobian M, Whittleston G (2022) A critical review of carbon nanomaterials applied in

685 cementitious composites – A focus on mechanical properties and dispersion techniques.
686 Alexandria Eng J 61:3417–3433. https://doi.org/10.1016/j.aej.2021.08.053

687 Yan J, Shamim T, Chou SK, et al (2017) Clean, efficient and affordable energy for a sustainable
688 future. Appl Energy 185:953–962. https://doi.org/10.1016/j.apenergy.2016.06.005

689 Yang L, Chen ZG, Dargusch MS, Zou J (2018) High Performance Thermoelectric Materials:
690 Progress and Their Applications. Adv Energy Mater 8:1–28.
691 https://doi.org/10.1002/aenm.201701797

692 Yao CJ, Zhang HL, Zhang Q (2019) Recent progress in thermoelectric materials based on
693 conjugated polymers. Polymers (Basel) 11:1–19. https://doi.org/10.3390/polym11010107

694 Zhang Y, Rhee KY, Park SJ (2019) Facile design of a domestic thermoelectric generator by
695 tailoring the thermoelectric performance of volume-controlled expanded graphite/PVDF
696 composites. Compos Part B Eng 176:107234.
697 https://doi.org/10.1016/j.compositesb.2019.107234

698 Zhao HD, Ling JM, Fu PC (2013) A review of harvesting green energy from road. In:
699 Advanced Materials Research. Trans Tech Publications Ltd, pp 559–566

700 Zheng S, Ni L, Liu H, Zhou H (2019) Measurement of the distribution of temperature and
701 emissivity of a candle flame using hyperspectral imaging technique. Optik (Stuttg)
702 183:222–231. https://doi.org/10.1016/j.ijleo.2019.02.077

703 Zhou Z, Wang X, Zhang X, et al (2015) Effectiveness of pavement-solar energy system - An
704 experimental study. Appl Energy 138:1–10.
705 https://doi.org/10.1016/j.apenergy.2014.10.045

706 Zuev YM, Chang W, Kim P (2009) Thermoelectric and magnetothermoelectric transport
707 measurements of graphene. Phys Rev Lett 102:1–4.
708 https://doi.org/10.1103/PhysRevLett.102.096807

709 Zuo J, Yao W, Wu K (2015) Seebeck effect and mechanical properties of carbon nanotube-
710 carbon fiber/cement nanocomposites. Fullerenes Nanotub Carbon Nanostructures
711 23:383–391. https://doi.org/10.1080/1536383X.2013.863760

Supplementary Files

This is a list of supplementary files associated with this preprint. Click to download.

- ESI.docx